Virtual lattice resonance of a single nanoresonator in a metal nanoslit

Ofer Doron [1,2,3] and Tal Ellenbogen[1,3]

[1]*Faculty of Engineering, Department of Physical Electronics, Tel Aviv University, Tel Aviv 69978, Israel*
[2]*Raymond and Beverly Sackler School of Physics & Astronomy, Tel Aviv University, Tel Aviv 69978, Israel*
[3]*Tel Aviv Center for Light-Matter Interaction, Tel Aviv University, Tel Aviv 69978, Israel*

We study the transmission through a subwavelength metallic slit loaded with a single nanoresonator. To gain physical insight into the problem a theoretical model combining the dipole approximation and image theory is developed. The model shows that the coupling between the single nanoresonator and the slit's cavity modes serves as a localized analog to an infinite nanoresonator array. This virtual array supports a surface image-lattice resonance due to the coherent self-scattering of the single nanoresonator. Thereby, it may lead to the ability to mimic many recently reported intriguing physical phenomena of real surface-lattice resonances in nanoresonator arrays, by a single-subwavelength system. We specifically show that it leads to enhanced light-matter interaction, and to the appearance of an extraordinary transmission window. The theoretical results are in good agreement with full-wave numerical simulations.

I. INTRODUCTION

In arrays of metallic nanoparticles (NPs), radiative coupling between the NPs was shown to drastically modify the effective single-NP response [1–7]. In particular, the coupling between the NPs' localized surface plasmon resonance (LSPR) and a photonic lattice mode, results in a hybridized state, named surface-lattice resonance (SLR). The SLR is characterized by sharp spectral features compared to the LSPR and is accompanied by large field enhancement in the vicinity of the NP. These characteristics enabled the utilization of the SLR phenomenon to demonstrate a variety of interesting and attractive physical phenomena. For example, it was used to demonstrate high-Q factors in plasmonic NP lattices [8–10], enhancement, and manipulation of nonlinear processes [11–14], coupling with different materials [15–17] that can lead to lasing [18,19], Bose-Einstein condensation [20,21], shaping and enhancing fluorescent emission [22,23], and sensing [24–26]. Furthermore, realization of SLRs in nontrivial lattices [27–32] and environments [33–37] enriches the hybridization picture with additional photonic modes and furthers the optical capabilities of the lattice. However, the SLR Q factor is highly influenced by edge effects [38], and thus large NP arrays are essential for demonstrating SLRs.

Another platform that was extensively studied for enhancing the light-matter interaction and facilitating a variety of physical phenomena is the Fabry-Perot (FP) cavity. By dressing the cavity with different emitters, strong coupling between photonic and material modes can be achieved [39–44]. Moreover, metallic NPs embedded between two horizontal metal films were shown to exhibit strong coupling between the plasmonic and the FP modes [45–52]. However, such systems were only demonstrated using coupling to longitudinal FP modes in a copropagation configuration, and the observed energy split is theoretically described by a Hamiltonian formalism, in analogy to quantum emitters. While the strong coupling characteristics are well captured by these models,

the details of the coupling process are hidden in the coupling-strength parameter.

In this paper, we theoretically and numerically demonstrate that a single resonant NP embedded in a horizontal FP cavity formed by a metallic subwavelength nanoslit locally mimics the optical response of an infinite NP chain. We employ the dipole approximation (DA) model, along with the method of images, to theoretically describe the coupling process between the single-NP resonance and the lateral FP cavity modes. Consequently, a virtual image-chain perspective replaces the interaction with the slit. The model shows that under the condition of coherent self-scattering the hybridized state shows similar features to that of an SLR on an infinite lattice. Therefore, it suggests that many of the recently discovered physical phenomena and applications of SLRs may be realized by a single-subwavelength nanoscale system [10–26].

Specifically, we show that the virtual image chain significantly enhances the light-matter interaction. This enhancement supports the transmission of light through the slit in the forbidden regime, above the cutoff wavelength of the bare slit (without the NP). We also show that unlike the conventional SLR phenomenon, the interaction may be further enhanced by large numerical aperture (NA) excitations [8]. To verify our model, we perform full-wave simulations of the proposed system using the finite-difference time-domain (FDTD) method.

II. RESULTS AND DISCUSSION

A. Theoretical model

The system we study is depicted in Fig. 1. A transverse electric (TE) polarized light normally illuminates an infinite gold film of height H, which contains a single infinitely long nanoslit of width W. A single gold nanorod of length l, width w, and thickness h is placed at the center of the slit. The ambient constant refractive index is n.
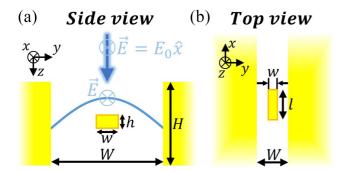
(a) **Side view**   (b) **Top view**

FIG. 1. Schematic illustration of the studied system as viewed from the side (a) and top (b). A TE polarized plane wave normally impinges on an infinite slit of width W, in a gold film of height H, in an ambient dielectric with refractive index n. A single gold nanorod, with width w, thickness h, and length l, is placed in the center of the slit. The impinging light's wave vector is in the z direction with the electric-field polarization in the x direction. In (a), the electric-field amplitude distribution along the y axis of the first FP cavity mode (of the bare slit) is shown inside the slit.

For the bare slit, assuming the metal is a perfect electric conductor (PEC) and ignoring the finite height of the slit, the tangential electric field at the slit boundaries must vanish and the electric-field profile inside the slit takes the form of an ideal waveguide:

$$\boldsymbol{E} = \sqrt{2}E_0\cos(k_{y,m}y)e^{-ik_{z,m}z}\hat{\boldsymbol{x}}, \qquad (1)$$

where E_0 is the impinging light's electric-field amplitude, $k_{y,m}$ and $k_{z,m} = \sqrt{k^2-k_{y,m}^2}$ are the y and z components of the wave vector of the mth mode, respectively, $m = 1, 2, \ldots$, $k = 2\pi n/\lambda$ is the impinging light's wave number, and λ is the vacuum wavelength.

The mth mode can propagate only if $k^2-k_{y,m}^2 > 0$; otherwise, $k_{z,m}$ is imaginary and the wave decays exponentially as it enters the slit, with a decay constant $|k_{z,m}|$. This defines the cutoff wavelength of the slit, above which no mode can propagate and is found from the condition $k_{z,1}^2 = 0$, resulting in

$$\lambda_{cutoff} = 2nW. \qquad (2)$$

Now, we turn to the loaded slit. To theoretically model the coupling process between the NP and the slit, we employ the DA along with the method of images. In the DA the NP is replaced by a point dipole, which is characterized by a polarizability α_s. In the presence of a local electric field E_{loc} a dipole moment p is excited:

$$p = \alpha_s E_{loc} = \alpha_s(E_{app} + E_{sca}), \qquad (3)$$

where the local field is the sum of E_{app}, the applied field, calculated from Eq. (1) at the dipole's location, and E_{sca}, the scattered field in the slit. The NP's elongated shape ensures that the dominant dipole moment is directed in the x direction, and the scalar approach may be invoked. We model the single-NP polarizability as a Lorentzian:

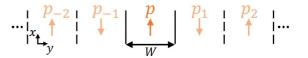$$\alpha_s(\omega) = \frac{A}{\omega_{LSPR}^2 - \omega^2 - i\gamma\omega}, \qquad (4)$$

FIG. 2. Schematic illustration of the infinite image chain. The basic unit cell is replicated an infinite number of times. The original dipole p (dipole images p_j) and unit-cell's boundaries (unit-cell's boundaries images) are marked by an orange arrow (light orange arrows) and solid black lines (dashed black lines), respectively. Alternating flipping of the arrows corresponds to a cumulative π phase shift according to Eq. (5), for the case of a PEC.

where A is the polarizability amplitude, $\omega = 2\pi c/\lambda$ is the optical angular frequency, c is the speed of light in vacuum, $\omega_{LSPR} = 2\pi c/\lambda_{LSPR}$ with λ_{LSPR} being the LSPR vacuum wavelength, and γ is the damping rate, which accounts for both Ohmic and scattering losses. For simplicity, we neglect corrections to the polarizability which account for full energy conservation and retardation effects of the dipole for the case of an elongated NP. For more accurate results, the modified long-wavelength approximation should be considered [53].

When light impinges on the slit, the dipole moment is excited by the applied field in Eq. (1), which can be propagating (for $k_z^2 > 0$) or decaying (for $k_z^2 < 0$) and reemits the radiation. Light radiated by the dipole in the y direction is reflected by the slit's boundaries back to the dipole in a self-scattering process. The slit's boundaries act as an infinity mirror such that an infinite number of reflections must be considered. Each reflection is characterized by a reflection amplitude R and phase φ_r (for a PEC $R = 1$ and $\varphi_r = \pi$).

To describe the reflections in the slit, we use the method of images. Figure 2 shows a schematic illustration of the excited-dipole moment p in the xy plane, along with its infinite images p_j, for $j = \pm 1, \pm 2, \ldots$. The jth image stems from $|j|$ reflections; thus, to account for the reflection amplitude and phase, the dipole moment takes the form

$$p_j = R^{|j|}e^{i|j|\varphi_r}p. \qquad (5)$$

The influence of each image on the original dipole is governed by Green's function formalism. In free space and under the scalar approximation, Green's function, which describes the emitted electric field from the jth image to the original dipole, takes the form

$$\mathcal{G}_j = e^{ikr_j}\left[\frac{(1-ikr_j)[3\cos^2(\vartheta_j)-1]}{r_j^3} + \frac{k^2\sin^2(\vartheta_j)}{r_j}\right], \qquad (6)$$

where $\boldsymbol{r}_j$ is the displacement vector from the image to the original dipole, $r_j = |\boldsymbol{r}_j| = |j|W$, and $\vartheta_j = 90°$ is the angle between the dipole moment and $\boldsymbol{r}_j$.

The total scattered field at the original dipole's location is given by the infinite sum over the scattered fields from all images:

$$E_{sca} = \sum_{j\neq 0}\mathcal{G}_j p_j = Sp; \quad S \equiv \sum_{j\neq 0}R^{|j|}e^{i|j|\varphi_r}\mathcal{G}_j, \qquad (7)$$

where S is the structural factor of the image chain and p_j was taken from Eq. (5).

The structural factor S describes the influence of the entire image chain on the original dipole and takes a similar form to the structural factor of an infinite NP chain under normal incidence illumination. For NP chains, the structural factor exhibits sharp resonances for the different orders of coherent scattering $\lambda_m^{(CS)} = nd/m$, with $\lambda_m^{(CS)}$ being the vacuum wavelength of the mth order of coherent scattering, d being the chain spacing, and $m = 1, 2, \ldots$. These coherent-scattering conditions are often referred to as Rayleigh anomalies, where a diffraction order of the chain propagates along the chain. Here, the structural factor exhibits sharp resonances under the conditions of coherent self-scattering. In the explicit form of the sum which defines S in Eq. (7), every term is multiplied by a complex exponent $\exp[i|j|(kW + \varphi_r)]$, such that the condition of coherent self-scattering is $k_m^{(CSS)}W + \varphi_r = 2\pi m$, where $m = 1, 2, \ldots$, and $k_m^{(CSS)} = 2\pi n/\lambda_m^{(CSS)}$, with $\lambda_m^{(CSS)}$ being the vacuum wavelength of the mth order of coherent self-scattering. For PEC boundary conditions $\varphi_r = \pi$, such that the orders of coherent self-scattering take the form $\lambda_m^{(CSS)} = nW/(m-1/2)$.

Comparison between the coherent scattering ($\lambda_m^{(CS)}$) and the coherent self-scattering ($\lambda_m^{(CSS)}$) orders reveals that for a certain wavelength, the coherent self-scattering modes occur for an image-chain spacing that is smaller than the corresponding NP chain spacing for coherent-scattering modes. For example, the first order of coherent self-scattering is achieved for an image-chain spacing that equals half the spacing of an NP chain at the coherent-scattering condition. As a result, the contribution of each image to the virtual structural factor is more significant, and the structural factor of an image chain reaches higher values than that of an NP chain. This leads to a stronger coupling between the single NP and the image chain, in resemblance to the increased coupling strength which occurs when increasing the polarizability amplitude [54].

It is interesting to see that the orders of coherent self-scattering $\lambda_m^{(CSS)}$ match the cutoff wavelengths of the odd TE waveguide modes in Eq. (1), which are found by taking $k_{z,m} = 0$, with $m = 1, 3, \ldots$. For each waveguide mode the corresponding cutoff wavelength separates between decaying (above the corresponding cutoff wavelength) and propagating (below the corresponding cutoff wavelength) waves of that mode, such that exactly at the cutoff wavelength a non-propagating mode may exist with no propagation or decay constants. These non-propagating modes correspond to the modes of coherent self-scattering of the NP, which may also be regarded as the FP cavity modes. Only odd FP cavity modes may interact with the NP owing to the reflection symmetry across the x-axis, and even FP cavity modes may be accessed by moving the NP from the center of the slit and breaking this symmetry.

Combining Eqs. (3)–(7) and solving for p results in

$$p = \alpha_{\mathrm{eff}}E_{\mathrm{app}}; \quad \alpha_{\mathrm{eff}} \equiv \frac{\alpha_s}{1 - S\alpha_s}, \qquad (8)$$

where α_{eff} is the effective polarizability of the point dipole in the presence of the slit, which is associated with the applied field rather than the local field.

This expression for the effective polarizability is a closed-form solution for the dipole's response in the slit and includes the influence of the image chain through the structural factor.

The image-chain perspective of the problem replaces the interaction with the slit, which is manifested in the model in the applied field, which is determined by the waveguide modes in Eq. (1), and in the reflection coefficients which appear in the structural factor. Equation (8) resembles the solution for an infinite array of dipoles [1] [Eq. (10) in Sec. IV, Methods]. In the context of NP arrays, the effective polarizability describes the collective response of the array, and within it the formation of an SLR. Here, the effective polarizability describes the hybridization of the LSPR and an FP cavity mode as the collective response of a virtual image chain. Under the condition of coherent self-scattering, the system manifests a subwavelength localized analog to the SLR phenomenon, which we name surface image-lattice resonance (SILR).

We note that for observing the SILR using the fundamental FP cavity mode, the height of the slit has a critical role in determining both the excitation strength of the dipole above the cutoff wavelength and the dissipation rate of the excited system. Above the cutoff wavelength of the bare slit, the applied field decays exponentially as it propagates in the slit, meaning that decreasing the height of the slit results in a stronger excitation of the dipole. For a strong enough excitation we look at the case of a subwavelength height. However, decreasing the height of the slit hinders its ability to mimic a mirror correctly. As the slit's height decreases to the subwavelength regime, the scattering from "far" images deviates from Green's function formalism such that only "close" images contribute significant coherent terms to the structural factor S, where the concept of far and close relates to the exact value of the slit height. As a result, the virtual photonic mode of coherent self-scattering, which is described by the structural factor, becomes increasingly dissipative. This is analogous to the low-Q factor of finite NP arrays as the size of the array is reduced [38].

These two competing roles of the slit's height put a limitation on the performance of the system. By setting a subwavelength height the excitation of the NP becomes sufficiently strong, with the cost of decreasing the Q factor of the resulting hybridized state. However, this limitation is unique to the fundamental mode of coherent self-scattering as it overlaps the cutoff condition of the bare slit. Higher modes of coherent self-scattering occur below the cutoff wavelength, such that the slit's height may be increased to achieve higher-Q factors without decreasing the excitation strength of the dipole.

Another inherent limitation for the system's Q factor is the reflection losses, which exist for all modes of coherent self-scattering. These reflection losses are negligible for scattering from images close to the original dipole and become pronounceable for "far" images, which suffer many losses due to the repeating reflections, where the definition of close and far is determined by the exact value of the reflection amplitude [Eq. (5)].

We note that these losses may be included in the model calculations by using the exact values of reflection amplitude and phase to calculate the structural factor in Eq. (7) and the corresponding coherent self-scattering conditions. Thus, this model suggests a general approach to embody the photonic modes of the cavity in the structural factor, regardless of the reflection coefficients, and to obtain an insightful closed-form
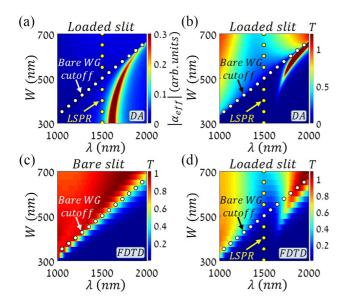
FIG. 3. (a) Absolute value of the effective polarizability α_{eff} (in arbitrary units), according to Eq. (8), as a function of wavelength λ and slit width W. Normalized transmission T as a function of wavelength λ and slit width W of (b) the loaded slit using the DA model, (c) Bare slit (without NP) using FDTD simulations, and (d) loaded slit using FDTD simulations. The bare slit's cutoff according to Eq. (2) is marked with white dots and the single-NP LSPR wavelength is marked with yellow dots at $\lambda_{\text{LSPR}} = 1500$ nm.

B. Numerical results

To observe the SILR dynamics we calculated the absolute value of the effective polarizability $|\alpha_{\text{eff}}|$ according to Eq. (8) (see Sec. IV, Methods) as a function of wavelength λ and slit width W, as presented in Fig. 3(a). The chosen Lorentzian parameters in Eq. (4) are $\lambda_{\text{LSPR}} = 1520$ nm, $\gamma = 314$ THz, and $A = 2.6 \times 10^{15}$ cm^3/s^2. These parameters were chosen to fit the response of the loaded slit obtained by full-wave simulations as described below. The reflection amplitude and phase were assumed to be of a PEC (i.e., $R = 1$ and $\varphi_r = \pi$) for simplicity, and the exact values of the reflection coefficients may be used for more accurate results.

It can be seen in Fig. 3(a) that the effective polarizability is greatly modified in comparison to the single-particle polarizability [Fig. 4(a) and Appendix], where the effective polarizability has a local minimum at the fundamental coherent self-scattering mode (which coincides with the cutoff wavelength and is marked with white dots), with an amplified, narrowed, and redshifted peak, and a diminished wide blueshifted peak surrounding it, in resemblance to SLRs [1,2].

It is interesting to compare between the SILR and SLR phenomena with respect to the resulting effective polarizability. Figure 4(b) depicts the absolute value of the effective polarizability of an infinite image chain (infinite NP chain) as a function of wavelength for a slit width of $W = 500$ nm
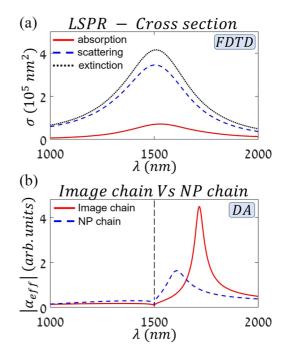

FIG. 4. (a) Absorption, scattering, and extinction cross sections σ of the single NP as a function of wavelength λ, in red solid line, blue dashed line, and black dotted line, respectively, using FDTD simulations. Extracted LSPR wavelength is about 1500 nm (see Appendix). (b) Absolute value of the effective polarizability α_{eff} as a function of wavelength λ for an image chain (red solid line) and for an infinite NP chain (blue dashed line), consisting of the same localized resonance. Effective polarizabilities were calculated according to the DA using Eqs. (8) and (10). Chain spacing was set to $W = 500$ nm for the image chain, and to $d = 1000$ nm for the NP chain, such the first orders of coherent (self-) scattering coincide at the LSPR wavelength of $\lambda = 1500$ nm (which is marked with a black dashed vertical line). The two effective polarizabilities show a similar behavior with three main differences. Polarizability peak of the image chain is stronger, narrower, and redshifted twice as much as the polarizability peak of the NP chain.

(chain spacing of $d = 1000$ nm), consisting of the same localized resonance. The image-chain and NP-chain spacings were chosen such that the first orders of coherent self-scattering (for the image chain) and coherent scattering (for the NP chain) coincide at the same wavelength of the LSPR, i.e., $\lambda = 1500$ nm. The resonance of the image chain is both stronger and narrower than the resonance of the NP chain. In addition, the resonance of the image chain peaks around a wavelength of 1700 nm, which translates to a spectral shift of $\sim$200 nm from the coherent self-scattering wavelength, which is double the spectral shift of the NP chain. These differences exhibit the increased coupling strength between the single NP and the image chain which occurs due to the shorter periodicity of the image chain, as described in the previous section. Namely, reduction of the chain spacing results with an enhanced structural factor which represents a stronger photonic mode. This increase in the coupling strength may be advantageous for the SILR compared to the SLR.

We also calculated the total transmitted energy through the loaded slit (see Sec. IV, Methods). Usually, the transmission

This solution for the effective polarizability in Eq. (8). This solution describes the coupling process between the NP and the cavity as hybridization of the NP and a chain of nonperfect images [Eq. (5)].

of light through NP arrays exhibits dips at the spectral location of the structure's resonances, which result from the absorption and reflection of the impinging energy at the array. However, for subwavelength metallic apertures transmission of light is typically forbidden (i.e., for $W < \lambda/2n$ in this case), and extraordinary optical transmission (EOT) peaks may appear when the structure's modes assist in channeling the impinging energy through the apertures [55–61]. Here, both regimes exist as explained below.

Figure 3(b) depicts the normalized transmission T through the loaded slit as a function of wavelength λ and slit width W, using the DA. The cutoff wavelength of the bare slit according to Eq. (2) is marked by white dots. Below the cutoff wavelength, transmission through the bare slit is allowed, and a transmission dip through the loaded slit exists due to energy dissipation and reflection, as in NP arrays. On the contrary, above the cutoff wavelength, transmission through the bare slit is forbidden, and the SILR leads the appearance of an EOT peak. This peak closely follows the curve of maximal $|\alpha_{\text{eff}}|$ in Fig. 3(a). Although the amplitude of the impinging light decays exponentially as it propagates through the slit, it still manages to excite the dipole located in the slit. The hybridized dipole then radiates to the exit of the slit, explaining the EOT features. In addition, the EOT peak shows a narrowed linewidth in accordance with the virtual collective-response picture.

One may expect that the EOT peak's amplitude will increase with increasing amplitude of α_{eff}; however, comparison of Fig. 3(a) with Fig. 3(b) shows a reversed amplitude profile. The maximal amplitude of α_{eff} is highest for small slit widths and decreases for increasing widths. On the contrary, the EOT peak is lowest for small slit widths and increases for increasing widths. This is because the decay constant $|k_z|$ increases as the cutoff wavelength and wavelength of maximal $|\alpha_{\text{eff}}|$ grow apart, and the impinging field's amplitude at the NP's location decreases exponentially. According to Fig. 3(a), this effect is most pronounced for small slit widths, and the excitation of the dipole is negligible. As the slit width increases the excitation of the dipole becomes powerful enough to support EOT.

To verify the theoretical model, we also performed full-wave FDTD simulations (see Sec. IV, Methods). Figure 3(c) depicts the normalized transmission T through the bare slit as a function of wavelength λ and slit's width W, using FDTD simulations. The white dots represent the cutoff of the bare waveguide, according to Eq. (2), which coincide with the visible cutoff in the graph. The simulated cutoff slightly deviates from the prediction for large slit widths. This is because of the subwavelength height of the slit, which leads to a field distribution that differs from the mode of an infinite height ideal waveguide, which appears in Eq. (1).

Figure 3(d) depicts the normalized transmission T through the loaded slit as a function of wavelength λ and slit width W, using FDTD simulations. It can be seen that Figs. 3(b) and 3(d) are in good agreement, where the EOT peak (above the cutoff wavelength) and the transmission dip (below the cutoff wavelength) follow the same trend, thus supporting the validity of the DA model.

Despite the overall agreement between the DA and FDTD calculations, the two graphs show two main differences: (1)
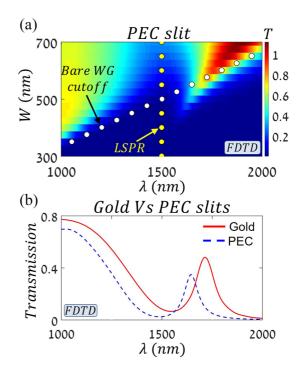

FIG. 5. Transmission through a loaded PEC slit. (a) Normalized transmission T through a loaded PEC slit as a function of wavelength λ and slit width W, using FDTD simulations. (b) Normalized transmission T through loaded PEC (dashed blue line) and gold (solid red line) slits as a function of wavelength λ, for a slit width of $W = 500$ nm, using FDTD simulations. Deviation of gold from a PEC leads to redshift, enhancement, and a reduced Q factor of the EOT peak.

The width of the EOT peak is narrower for the DA calculation compared to FDTD calculation, and (2) at long wavelengths, the transmission calculated by the DA shows a dip along the cutoff condition, which is absent from the FDTD calculation. The former may be explained due to the subwavelength height of the slit, as explained in the previous section, and due to losses, which inherently exist in reflections from gold in the FDTD simulations, and contrasts with the PEC assumption which was taken in the DA calculations. The latter may be explained by the subwavelength height of the slit, which creates deviations from the ideal waveguide assumption that was taken in the DA calculations.

To better understand the loss mechanism in the FDTD simulations, we simulated a loaded PEC slit, where the slit was made from a PEC instead of gold (see Sec. IV, Methods). The NP remains the same, i.e., made of gold, such that only losses attributed to the repeating reflections in the slit are omitted from the calculations. The remaining losses result from the NP and the finite height of the slit. Figure 5(a) depicts the normalized transmission through the loaded PEC slit as a function of slit width W and wavelength λ, using FDTD simulations. This transmission plot is very similar to Fig. 3(d) and shows the same characteristics, with some disagreement on the spectral location of the features.

Figure 5(b) depicts the transmission through the loaded slit as a function of wavelength λ, for gold and PEC slits, with a width of $W = 500$ nm. The transmission through the

two loaded slits shows very similar behavior, with an EOT peak above the cutoff wavelength and a transmission dip below. However, the EOT peak of the gold slit is redshifted by ~50 nm from the EOT peak of the PEC slit. While the repeating reflections in the PEC slit occur with a reflection phase of $\varphi_r = \pi$, the reflections in the gold slit are characterized by a reflection phase slightly larger than π. This small phase addition for the gold slit is introduced into the coherent self-scattering condition and consequently redshifting it by a small amount, which in turn redshifts the SILR. In addition, the EOT peak of the gold slit is stronger, which is attributed to a smaller decay constant of the applied field, due to the deviation from a PEC behavior.

In order to assess the reflection losses in the gold slit we calculated the Q factor of the two SILRs using $Q = \lambda_{\mathrm{res}}/\Delta\lambda$, with λ_{res} being the wavelength of maximal transmission and $\Delta\lambda$ being the SILR width at half maximum. The SILR Q factors of the PEC and gold slits are found to be $Q_{\mathrm{PEC}} \approx 19.5$ and $Q_{\mathrm{gold}} \approx 14.5$, respectively, where the decrease in the Q factor is caused by the reflection losses of gold. The increased dissipation shown in the gold simulations may pose limitations on the performance of the SILR when extremely high-Q factors are required. However, a Q factor of ~15 corresponds to quadrupling of the Q factor compared with the LSPR [calculated according to Fig. 4(a)], depicting the pronounced influence of the image chain on the effective response of the NP. Additionally, by working with higher modes of coherent self-scattering such that the height of the slit may be increased, and by adding a periodicity of NPs within the slit, the Q factor of the SILR may be increased.

We also examined the electric-field enhancement inside the slit. Figures 6(a) and 6(b) depicts the electric field's normalized amplitude profile in the xy plane, on top of the NP, for the loaded slit (with a width of $W = 500$ nm, at the EOT wavelength) and an isolated NP (at the LSPR wavelength), respectively, using FDTD simulations. The electric field's amplitude in the loaded slit at the vicinity of the NP shows up to 70-fold enhancement compared to the applied field amplitude, ~3 times higher than the enhancement around the single NP at its resonance, suggesting that the proposed system may be beneficial for nonlinear applications and light-matter coupling, in similarity to SLRs [10–26].

In addition, we examined the effect of varying the angle of incidence of the impinging light on the SILR. Figure 7(a) [Fig. 7(c)] shows a schematic illustration of the slit under oblique incidence illumination, at an angle φ in the yz plane (angle ψ in the xz plane). Figure 7(b) [Fig. 7(d)] depicts the normalized transmission T through the loaded slit as a function of wavelength λ and angle of incidence $\varphi(\psi)$, for a constant slit width $W = 500$ nm. The transmission plots reveal that while the EOT amplitude diminishes for increasing angles of incidence, the spectral location of the EOT peak, and therefore also of the SILR, remains constant. In contrast to arrays of NPs, where coherent scattering highly depends on the angle of incidence [4,18], our proposed system holds the condition for coherent self-scattering constant, regardless of the angle of incidence. The impinging light couples to the waveguide modes of the bare slit, which are predetermined by the geometry. The decrease in EOT peak's amplitude is mainly due to decrease in the coupling strength between the
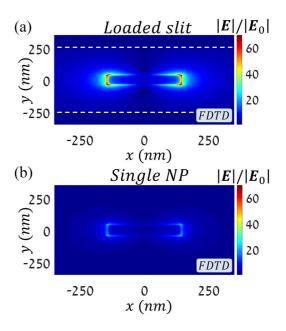

FIG. 6. Electric-field amplification in the xy plane, on top of the nanorod, for (a) loaded slit of width of $W = 500$ nm at the EOT wavelength, and (b) an isolated nanorod at the LSPR wavelength at $\lambda = 1550$ nm, using FDTD simulations. The two plots are displayed in the same scale for comparison, and in (a) white dashed lines indicate the slit's boundaries. Electric-field enhancement in the loaded slit is ~3 times higher than the field enhancement around the isolated nanorod.

impinging light and the waveguide modes of the bare slit, which may be understood by the reduced effective field of view of the slit for oblique illumination. In addition, increasing the angle ψ results in quicker decay compared to the
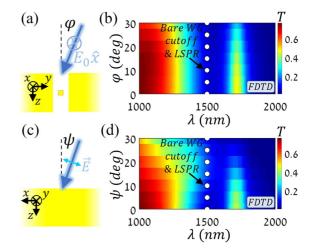

FIG. 7. Oblique incidence illumination. Schematic illustration of the slit under oblique incidence illumination, at (a) an angle φ in the yz plane, and (c) angle ψ in the xz plane. Normalized transmission spectrum T through the loaded slit (with a width of $W = 500$ nm) as a function of (b) angle of incidence φ, and (d) angle of incidence ψ, using FDTD simulations. Cutoff wavelength according to Eq. (2) and LSPR wavelength are marked with white dots at $\lambda = 1500$ nm. EOT peak strength diminishes with increasing angles of incidence, however the spectral location is unchanged.
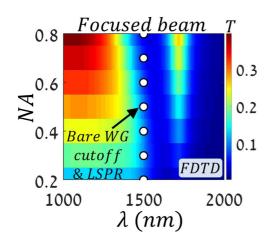
FIG. 8. Focused-beam illumination. Transmission T through the loaded slit under a Gaussian-beam illumination as a function of wavelength λ and NA, with a slit width of $W = 500$ nm, using FDTD simulations. Observed EOT peak reaches up to ~ 0.25 for high NA values.

φ dependence. This is due to the difference of the light's polarization for the two cases. For angle φ, the polarization of the impinging light remains the same, in the x axis. However, for angle ψ, the polarization rotates in the xz plane such that the effective exciting field (i.e., only the x component) is reduced.

This angle-independence behavior raises the possibility of experimentally measuring the predicted transmission using a focused beam, in contrast to an SLR in NP arrays [8]. Such a configuration has the potential to measure the SILR from a single NP, and to highly enhance the light-matter interactions. As a proof of concept, we calculated Fig. 8, which depicts the transmission spectrum T through the loaded slit as a function of NA for a Gaussian beam illumination, using FDTD simulations. The EOT peak is relatively weak for small NAs and enhances with increasing NA values, as expected since the impinging spot size decreases with increasing NA. The EOT strength reaches ~ 0.25 for a highly focused beam. In addition, focusing of the impinging light increases the applied field concentration, which translates to an increase in the field enhancement around the NP.

III. CONCLUSIONS

In conclusion, we have theoretically and numerically investigated the transmission of light through a subwavelength metal slit loaded with a resonant NP under TE illumination. To study the coupling process between the FP cavity and the NP we used a DA approach combined with image theory. The model analysis resulted in a closed-form solution for the effective polarizability, which accounts for infinite reflections in the cavity and describes the hybridization of the LSPR and an FP cavity mode, which gives rise to an SILR mode. The effective polarizability resembles the solution for an infinite NP array, such that the SILR acts as a localized subwavelength analog to the well-known long-ranged SLR. The SILR supports enhancement of the effective polarizability which aids the transmission of the impinging energy through

the slit in the forbidden-wavelength regime, resulting with an EOT peak, which exhibits a Q factor ~ 4 times larger than the LSPR's. We verified the theoretical model using full-wave FDTD simulations, which showed the predicted existence of the EOT effect as well as a significant field enhancement at the SILR condition. We also investigated the effect of varying the angle of incidence on the SILR. Our results suggest that it may be possible to experimentally demonstrate the predicted SILR using a single NP and a focused beam, and that the proposed system may find applications in enhancing light-matter interactions and nonlinear optics, in analogy to NP arrays [10–26], but with a single-subwavelength system. In addition, the presented theoretical model may be easily expanded for NP arrays in an FP cavity in different configurations, such that the strong coupling observed in such systems [45–52] may be understood by our microscopic theoretical framework, rather than the use of the macroscopic coupling-strength parameter.

IV. METHODS

Numerical calculations

In order to calculate the effective polarizability in Eq. (8) and avoid divergence of the values, the structural factor in Eq. (7) was calculated as a finite sum over N images from each side of the central dipole. This finite sum is an approximation for the infinite sum in Eq. (7), where above a certain N value, addition of more terms to the finite sum will slowly increase the structural factor's absolute value without changing the spectral location of its resonance. In practice, for $N \geqslant 5000$ the calculated structural factor changes very little with increasing N such that the calculations were made with $N = 10\,000$.

In addition, the DA was used to calculate the normalized transmitted energy through the slit. The electric field at the exit surface of the slit is calculated as the sum of the applied field and the scattered fields from the infinite image chain in Fig. (2). The applied field was taken from Eq. (1), where the corresponding k_z accounts for propagating or decaying waves, and the scattered fields were calculated according to Green's function formalism. The exit surface of the slit was set at $z = H/2$ and has a size of the slit width at the y axis and the size in the x axis was set to 1350 nm in order to match the results retrieved from full-wave simulations. The exit surface was divided into 25×25 equally spaced grid points. The total scattered field $E_{\mathrm{sca},l}$ to each point l from the image chain was calculated using

$$E_{\mathrm{sca},l} = \sum_{j=-N}^{N} R^{|j|} e^{i|j|\varphi_r} \mathcal{G}(|\boldsymbol{r}_l - \boldsymbol{r}_j|) p, \qquad (9)$$

where $\mathcal{G}(|\boldsymbol{r}_l - \boldsymbol{r}_j|)$ is Green's function between the jth dipole image at location $\boldsymbol{r}_j = jW\hat{\boldsymbol{x}}$ and the relevant point at $\boldsymbol{r}_l$. For $j = 0$ the sum includes the direct scattering from the original dipole at the origin. The number of images on each side was set to $N = 5000$, thus neglecting the contribution of further images.

To compare between the effective polarizabilities of the loaded slit and an infinite NP chain [Fig. 4(b)], we calculated the effective polarizability of the infinite NP chain according

to [1]

$$\alpha_{\mathrm{eff,chain}} = \frac{\alpha_s}{1 - S_{\mathrm{chain}}\alpha_s}; \; S_{\mathrm{chain}} = \sum_{j \neq 0} \mathcal{G}_j, \qquad (10)$$

where S_{chain} is the structural factor of the NP chain, which was calculated using a finite sum instead of an infinite sum, including $N = 10\,000$ closest NPs from each side.

To verify the theoretical model, we performed full-wave FDTD simulations (LUMERICAL). The dielectric permittivity of gold was fitted to data from Ref. [62], and a constant background index of $n = 1.5$ was set. For simulating the PEC slit (Fig. 5), the permittivity of the slit was set to $\varepsilon_{\mathrm{PEC}} = 1 + i \times 10^6$. The slit height and NP length, width, and thickness were set throughout the paper to $H = 750$ nm, $l = 275$ nm, $w = 70$ nm, and $h = 50$ nm, respectively. Perfectly matched layer boundary conditions were set for all boundaries. The normalized transmission is measured at the exit of the slit, as the energy emerging from the slit divided by the energy impinging the slit area. The slit area was defined to have the size of the slit's width in the y axis and the size of the x direction was set to 2000 nm.

For a Gaussian beam illumination, the lens diameter and beam diameter at the lens were set to 5 and 4 mm, respectively. The beam normally impinges the slit at its focal point. The transmission was calculated as the total energy emerging from the slit divided by the total impinging energy (not normalized to the slit area).

APPENDIX: LOCALIZED SURFACE PLASMON RESONANCE

Figure 4(a) depicts the absorption, scattering, and extinction cross sections σ of a single gold nanorod as a function of wavelength, using finite-difference time-domain simulations. The nanorod's geometrical constants are $l = 275$ nm, $w = 70$ nm, and $h = 50$ nm, and the surrounding refractive index is $n = 1.5$. All three cross sections depict a typical behavior for an LSPR [1], characterized with broad resonances, which are around the same wavelength. The nanorod exhibits large scattering efficiency compared to the absorption, making the radiative damping the dominant source of the resonance, which is manifested in the extinction cross section. The LSPR wavelength is determined by the spectral location of the maximal value of the extinction cross section, around $\lambda = 1500$ nm.

[1] B. Auguié and W. L. Barnes, Phys. Rev. Lett. **101**, 143902 (2008).

[2] Y. Chu, E. Schonbrun, T. Yang, and K. B. Crozier, Appl. Phys. Lett. **93**, 181108 (2008).

[3] A. D. Humphrey and W. L. Barnes, Phys. Rev. B **90**, 075404 (2014).

[4] J. P. Martikainen, A. J. Moilanen, and P. Törmä, Philos. Trans. R. Soc., A **375**, 20160316 (2017).

[5] F. J. García de Abajo, Rev. Mod. Phys. **79**, 1267 (2007).

[6] A. Vaskin, R. Kolkowski, A. F. Koenderink, and I. Staude, Nanophotonics **8**, 1151 (2019).

[7] V. G. Kravets, A. v. Kabashin, W. L. Barnes, and A. N. Grigorenko, Chem. Rev. **118**, 5912 (2018).

[8] M. S. Bin-Alam *et al.*, Nat. Commun. **12**, 974 (2021).

[9] F. Yan, Q. Li, Z. Wang, H. Tian, and L. Li, Opt. Express **29**, 7015 (2021).

[10] M. J. Huttunen, O. Reshef, T. Stolt, K. Dolgaleva, R. W. Boyd, and M. Kauranen, J. Opt. Soc. Am. B **36**, E30 (2019).

[11] S. Linden, F. B. P. Niesler, J. Förstner, Y. Grynko, T. Meier, and M. Wegener, Phys. Rev. Lett. **109**, 015502 (2012).

[12] L. Michaeli, S. Keren-Zur, O. Avayu, H. Suchowski, and T. Ellenbogen, Phys. Rev. Lett. **118**, 243904 (2017).

[13] M. J. Huttunen, P. Rasekh, R. W. Boyd, and K. Dolgaleva, Phys. Rev. A **97**, 053817 (2018).

[14] O. Doron, L. Michaeli, and T. Ellenbogen, J. Opt. Soc. Am. B **36**, E71 (2019).

[15] M. Ramezani, M. Berghuis, and J. G. Rivas, J. Opt. Soc. Am. B **36**, E88 (2019).

[16] R. Kolkowski and A. F. Koenderink, Proc. IEEE **108**, 795 (2020).

[17] D. Wang, J. Guan, J. Hu, M. R. Bourgeois, and T. W. Odom, Acc. Chem. Res. **52**, 2997 (2019).

[18] T. K. Hakala, H. T. Rekola, A. I. Väkeväinen, J.-P. Martikainen, M. Nečada, A. J. Moilanen, and P. Törmä, Nat. Commun. **8**, 13687 (2017).

[19] A. Yang, T. B. Hoang, M. Dridi, C. Deeb, M. H. Mikkelsen, G. C. Schatz, and T. W. Odom, Nat. Commun. **6**, 6939 (2015).

[20] J.-P. Martikainen, M. O. J. Heikkinen, and P. Törmä, Phys. Rev. A **90**, 053604 (2014).

[21] T. K. Hakala, A. J. Moilanen, A. I. Väkeväinen, R. Guo, J.-P. Martikainen, K. S. Daskalakis, H. T. Rekola, A. Julku, and P. Törmä, Nat. Phys. **14**, 739 (2018).

[22] G. Vecchi, V. Giannini, and J. Gómez Rivas, Phys. Rev. Lett. **102**, 146807 (2009).

[23] F. Laux, N. Bonod, and D. Gérard, J. Phys. Chem. C **121**, 13280 (2017).

[24] B. Špačková and J. Homola, Opt. Express **21**, 27490 (2013).

[25] D. C. Hooper, C. Kuppe, D. Wang, W. Wang, J. Guan, T. W. Odom, and V. K. Valev, Nano Lett. **19**, 165 (2019).

[26] A. Danilov, G. Tselikov, F. Wu, V. G. Kravets, I. Ozerov, F. Bedu, A. N. Grigorenko, and A. V. Kabashin, Biosens. Bioelectron. **104**, 102 (2018).

[27] R. Guo, T. K. Hakala, and P. Törmä, Phys. Rev. B **95**, 155423 (2017).

[28] S. Baur, S. Sanders, and A. Manjavacas, ACS Nano **12**, 1618 (2018).

[29] L. Zundel, A. May, and A. Manjavacas, ACS Photonics **8**, 360 (2021).

[30] I. M. Fradkin, S. A. Dyakov, and N. A. Gippius, Phys. Rev. Appl. **14**, 054030 (2020).

[31] I. M. Fradkin, S. A. Dyakov, and N. A. Gippius, Phys. Rev. B **102**, 045432 (2020).

[32] D. Ben-Haim and T. Ellenbogen, Laser Photon. Rev. 2200671 (2023).

[33] A. Berkhout and A. F. Koenderink, ACS Photonics **6**, 2917 (2019).

[34] D. ben Haim, L. Michaeli, O. Avayu, and T. Ellenbogen, Opt. Express **28**, 17923 (2020).

[35] O. Reshef, M. Saad-Bin-Alam, M. J. Huttunen, G. Carlow, B. T. Sullivan, J. M. Ménard, K. Dolgaleva, and R. W. Boyd, Nano Lett. **19**, 6429 (2019).

[36] T. Abir, M. Tal, and T. Ellenbogen, Nano Lett. **22**, 2712 (2022).

[37] M. Sharma, L. Michaeli, D. Ben-Haim, and T. Ellenbogen, ACS Photonics **9**, 2702 (2022).

[38] S. R. K. Rodriguez, M. C. Schaafsma, A. Berrier, and J. Gómez Rivas, Physica B **407**, 4081 (2012).

[39] Y. Kaluzny, P. Goy, M. Gross, J. M. Raimond, and S. Haroche, Phys. Rev. Lett. **51**, 1175 (1983).

[40] A. Vukics and P. Domokos, Phys. Rev. A **86**, 053807 (2012).

[41] H. Kimble, Phys. Scr. **127**, T76 (1998).

[42] C. J. Hood, M. S. Chapman, T. W. Lynn, and H. J. Kimble, Phys. Rev. Lett. **80**, 4157 (1998).

[43] F. Brennecke, T. Donner, S. Ritter, T. Bourdel, M. Köhl, and T. Esslinger, Nature (London) **450**, 268 (2007).

[44] A. Ridolfo, M. Leib, S. Savasta, and M. J. Hartmann, Phys. Rev. Lett. **109**, 193602 (2012).

[45] A. Konrad, A. M. Kern, M. Brecht, and A. J. Meixner, Nano Lett. **15**, 4423 (2015).

[46] R. Ameling and H. Giessen, Nano Lett. **10**, 4394 (2010).

[47] R. Ameling and H. Giessen, Laser Photonics Rev. **7**, 141 (2013).

[48] J. Chen, Q. Zhang, C. Peng, C. Tang, X. Shen, L. Deng, and G.-S. Park, IEEE Photonics Technol. Lett. **30**, 728 (2018).

[49] A. Bisht, J. Cuadra, M. Wersäll, A. Canales, T. J. Antosiewicz, and T. Shegai, Nano Lett. **19**, 189 (2019).

[50] D. G. Baranov, B. Munkhbat, E. Zhukova, A. Bisht, A. Canales, B. Rousseaux, G. Johansson, T. J. Antosiewicz, and T. Shegai, Nat. Commun. **11**, 2715 (2020).

[51] Y. Shi, W. Liu, S. Liu, T. Yang, Y. Dong, D. Sun, and G. Li, Photonics **9**, 84 (2022).

[52] Y. Shi, Y. Dong, D. Sun, and G. Li, Materials **15**, 1523 (2022).

[53] T. Jensen, L. Kelly, A. Lazarides, and G. C. Schatz, J. Clust. Sci. **10**, 295 (1999).

[54] L. Michaeli, H. Suchowski, and T. Ellenbogen, Laser Photonics Rev. **14**, 1900204 (2020).

[55] T. W. Ebbesen, H. J. Lezec, H. F. Ghaemi, T. Thio, and P. A. Wolff, Nature (London) **391**, 667 (1998).

[56] A. G. Borisov, F. J. Garcia de Abajo, and S. V. Shabanov, Phys. Res. B **71**, 075408 (2005).

[57] S. G. Rodrigo, F. J. García-Vidal, and L. Martín-Moreno, Phys. Rev. B **77**, 075401 (2008).

[58] M. J. Kofke, D. H. Waldeck, Z. Fakhraai, S. Ip, and G. C. Walker, Appl. Phys. Lett. **94**, 023104 (2009).

[59] Y.-J. Bao, R.-W. Peng, D.-J. Shu, M. Wang, X. Lu, J. Shao, W. Lu, and N.-B. Ming, Phys. Rev. Lett. **101**, 087401 (2008).

[60] E. A. Shaner, J. G. Cederberg, and D. Wasserman, Appl. Phys. Lett. **91**, 181110 (2007).

[61] R. Gordon, D. Sinton, K. L. Kavanagh, and A. G. Brolo, Acc. Chem. Res. **41**, 1049 (2008).

[62] E. D. Palik, *Handbook of Optical Constants of Solids* (Academic Press, New York, 1980).